

Determination of protein structural flexibility by microsecond force spectroscopy

Mingdong Dong, Sudhir Husale and Ozgur Sahin*

Proteins are dynamic molecular machines having structural flexibility that allows conformational changes^{1,2}. Current methods for the determination of protein flexibility rely mainly on the measurement of thermal fluctuations and disorder in protein conformations^{3–5} and tend to be experimentally challenging. Moreover, they reflect atomic fluctuations on picosecond timescales, whereas the large conformational changes in proteins typically happen on micro- to millisecond timescales^{6,7}. Here, we directly determine the flexibility of bacteriorhodopsin—a protein that uses the energy in light to move protons across cell membranes—at the microsecond timescale by monitoring force-induced deformations across the protein structure with a technique based on atomic force microscopy. In contrast to existing methods, the deformations we measure involve a collective response of protein residues and operate under physiologically relevant conditions with native proteins.

The two-way coupling between protein chemistry and mechanics demands an understanding of the local flexibility of the protein structure so that a more accurate structure–function relationship can be established⁸. Atomic force microscope (AFM) based force spectroscopy is routinely used for mechanical property measurements of biological samples and exploring energy landscapes of proteins by stretching and unfolding single molecules^{9–12}. However, the native conformations of proteins span an infinitesimal fraction of their entire configuration space. Therefore, probing the flexibility of proteins in their native conformation requires constraining the deformations in the protein structure to a few angstroms.

Recently, specially designed torsional harmonic cantilevers (THC) have been developed to perform high-speed force spectroscopic measurements while scanning the surface in tapping-mode AFM¹³. Owing to the offset location of the sharp tip seen in Fig. 1a, the torsional vibrations of this cantilever are sensitive to the forces on the vertically oscillating tip. To enable operation of this method in liquids with forces gentle enough to investigate proteins, we have redesigned the cantilever geometry and reduced its flexural and torsional force constants. Hereafter, we will refer to this new design as an L-THC (liquid torsional harmonic cantilever). Vibration spectra recorded in aqueous buffer (shown in Fig. 1b) demonstrate the ability of the torsional mode to enhance harmonic signals in liquids. Multifrequency excitation and detection of cantilever vibrations have proven to improve spatial resolution of imaging in liquid environments^{14,15}. The advantage of the enhancement of multiple harmonic signals with the L-THC is the ability to recover the tip–sample force waveforms shown in Fig. 1c, which provide high-speed force–distance curves and allow specific material properties to be measured with high spatial resolution. Note that the entire period of the tip–sample force waveform in Fig. 1c is ~ 130 μ s and the interactions span 20 μ s. Furthermore, the waveform exhibits an rms. force noise of ~ 10 pN. This represents more than three orders of magnitude improvement in force sensitivity compared to the measurements performed with conventional cantilevers

in liquid¹⁶. This advance enabled a reduction in the peak interaction forces to allow investigations of various types of proteins without causing them to be denatured. In addition, owing to the microsecond duration of force loading, the mechanical properties derived from these waveforms will reflect molecular behaviour at the microsecond timescale. We therefore refer to these mechanical measurements as microsecond force spectroscopy.

We have investigated the flexibility of bacteriorhodopsin (bR), a light-driven proton pump forming the purple membranes of *Halobacterium salinarum*¹⁷. bR goes through large conformational changes during its photochemical cycle^{6,7}, and is responsible for controlling proton conduction from the cytoplasm to the active site of the protein containing retinal¹⁸. Measurements of force-induced deformations on both the cytoplasmic and extracellular sides of the purple membrane with our AFM-based technique can help determine the flexibility of bR, as well as the lipids surrounding them.

Using the L-THC we scanned purple membrane patches adsorbed onto a mica substrate in the tapping mode and generated topography, phase and flexibility maps, simultaneously. Figure 2a shows a tapping-mode topography image of two adjacent membrane patches. The corresponding height profile in Fig. 2f reveals different apparent thicknesses for these membranes of 5.7 and 7.2 nm, respectively. This contrast, manifested by the effect of electrostatic interactions¹⁹, allows the cytoplasmic and extracellular surfaces to be distinguished²⁰. The higher surface charge of the cytoplasmic side leads to an increased apparent height as observed with the membrane patch on the top side of Fig. 2a. The phase image, which is conventionally known to be sensitive to material contrast, does not show any noticeable differences between the two adjacent patches (Fig. 2b,g).

We generated the flexibility map by analysing the high-speed force–distance curves obtained at each pixel during the tapping-mode imaging process. Local reduced elastic modulus values are approximated by fitting these curves against a contact mechanics model (see Methods). The flexibility map in Fig. 2c exhibits a surprisingly clear contrast between the membrane patches. The numerical values plotted in Fig. 2h show that the reduced elastic modulus of the extracellular side is nominally 35 MPa, whereas the cytoplasmic side is measured to be 7 MPa. The accuracies of these values are primarily limited by the accuracy of cantilever spring constant calibration²¹, which can introduce an error on the order of 10%. In addition, the data in Fig. 2h show that the elastic modulus values recorded on the extracellular and cytoplasmic sides range between 15–50 MPa and 4–10 MPa, respectively. This variation is both related to the noise in force measurements and the heterogeneity in mechanical properties of lipids and proteins.

To observe molecular details in the flexibility map, we have analysed the two patches with higher resolution. Figure 2d,e presents flexibility maps obtained by scanning regions marked with ‘CP’

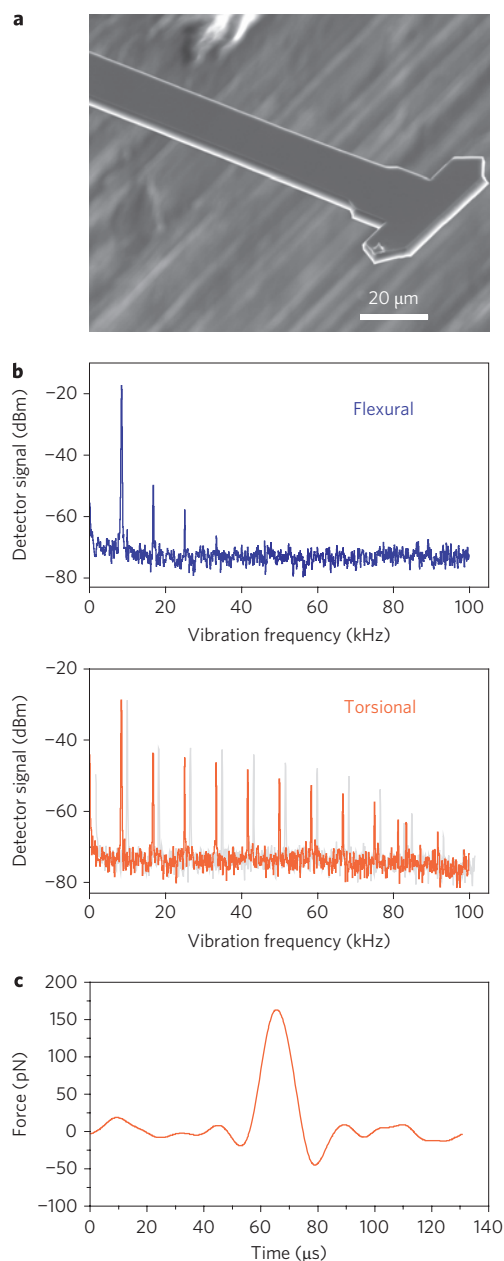


Figure 1 | Microsecond force spectroscopy in liquids. **a**, A scanning electron micrograph (SEM) image of a liquid torsional harmonic cantilever (L-THC). **b**, Flexural and torsional vibration spectra of an L-THC tapping on a purple membrane sample in aqueous buffer. A torsional spectrum on a mica sample is shown in light grey to show the differences in the magnitudes of high-frequency peaks in the different materials. For clarity, the spectrum on mica is offset by 2 kHz to the right. **c**, A tip-sample force waveform recovered from the torsional vibrations.

and 'EC' in Fig. 2c. Both images resolve the bR trimers arranged in a hexagonal lattice with ~ 6 nm spacing. The triangular morphologies of the trimers are also visible. The regions between the trimers, occupied by lipids, exhibit reduced elastic moduli lower than the proteins. The elastic modulus values recorded on the lipid regions are approximately 5 MPa on the cytoplasmic side and 16 MPa on the extracellular side. The higher value for the lipids on the extracellular side is likely a consequence of the lateral interactions coupling from the stiffer protein regions on the same side of the membrane. We believe the resolution of these measurements is

limited by the relatively high spring constant of the L-THC (0.18 N m^{-1}) compared to typical values for conventional cantilevers used in fluid tapping mode.

In the above analysis of the flexibility images, we reduced the rich tip-sample interaction to a single elastic modulus parameter. The reliability of this parameter is limited by the applicability of continuum models that predict force-distance relationships between macroscopic objects in contact. Non-uniformities and voids²² in the protein architecture or gaps between the membrane and the solid support can have a considerable effect on the measured flexibilities. In addition, surface roughness can result in changes in contact areas, which also influences phase images²³.

One can reach a better and more detailed understanding of local flexibility as well as other molecular interactions by investigating the complete force-distance curves, because interaction components such as van der Waals forces, screened electrostatic interactions and mechanical restoration forces have different spatial dependencies. Figure 3a presents force-distance curves that belong to the two sides of the purple membrane and mica. We have divided the graph into three regions to illustrate where the tip and sample are separated (I), and where they are interacting through long-range (II) and short-range forces (III). The buffer conditions used in this experiment lead to repulsive electrostatic forces on each sample with a screening length of ~ 0.55 nm. Therefore, region II reveals a competition between the attractive van der Waals forces and repulsive electrostatic forces. We see that the forces measured on each sample in this region follow the same order of surface charge densities expected from these samples, that is, from high to low: cytoplasmic side, extracellular side and mica^{20,24}.

The information regarding the local flexibility of the sample resides in region III of Fig. 3a where the tip is in direct contact with the sample. The repulsive interaction forces lead to angstrom-scale deformations in the sample surface, which have been visualized by the topographical images in contact-mode AFM^{25,26}. In this interaction region, the variation of tip-sample forces is determined mainly by the local flexibility of the sample. In fact, the short-range nature of these mechanical restoration forces makes it possible to generate flexibility maps with high spatial resolution as seen in Fig. 2d,e. One can describe local flexibility in a simpler way with effective force constants that can be obtained from the slopes of the curves in region III. From the data in Fig. 3a we obtained 0.13 N m^{-1} for the cytoplasmic side, 0.39 N m^{-1} for the extracellular side and 2.25 N m^{-1} for the mica substrate.

We carried out additional flexibility measurements on the two sides of the purple membranes under different buffer conditions. Although measurements in buffers with 300 mM and 1 M salt (KCl) concentrations at a constant pH of 7.8 did not show noticeable differences in stiffness, changing the pH of the imaging buffer resulted in changes in the effective force constants. Table 1 shows average force constants and their variation observed on each region of the sample at three pH levels. From the data we see that the apparent stiffnesses on either side of the membrane slightly increase with increasing pH and that the stiffness contrast is more dramatic at pH 6 (flexibility maps and force-distance curves for these measurements are provided in the Supplementary Information). The pH-dependent analysis of effective force constants reflects the utility of our AFM-based approach in that it allows probing of the flexibility of membrane proteins in a range of biologically relevant conditions.

The differentiation of the flexibility of cytoplasmic and extracellular sides and the nanometre-scale lateral resolution observed in the flexibility maps are enabled by the confinement of mechanical interactions to the vicinity of the contact region in AFM, as illustrated in Fig. 3b. The measured flexibility is therefore determined predominantly by the collective response of the protein residues and lipids within this interacting volume. The observed flexibility contrast

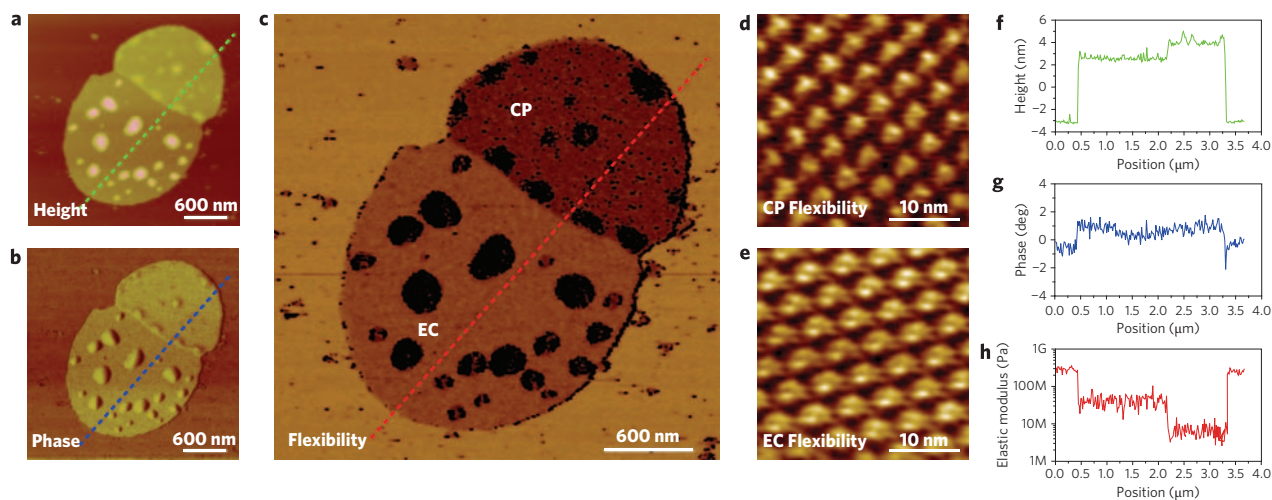


Figure 2 | High-resolution mapping of protein flexibility. **a–c**, Height (**a**), phase (**b**) and quantitative flexibility (**c**) maps of two adjacent patches of purple membranes. The scan size is $3.2 \times 3.2 \mu\text{m}^2$. **d,e**, High-resolution flexibility maps of the cytoplasmic (**d**) and extracellular (**e**) sides obtained from the regions indicated by CP and EC in **c**. **f–h**, Numerical values plotted from left to right across the dashed lines in **a–c**, respectively.

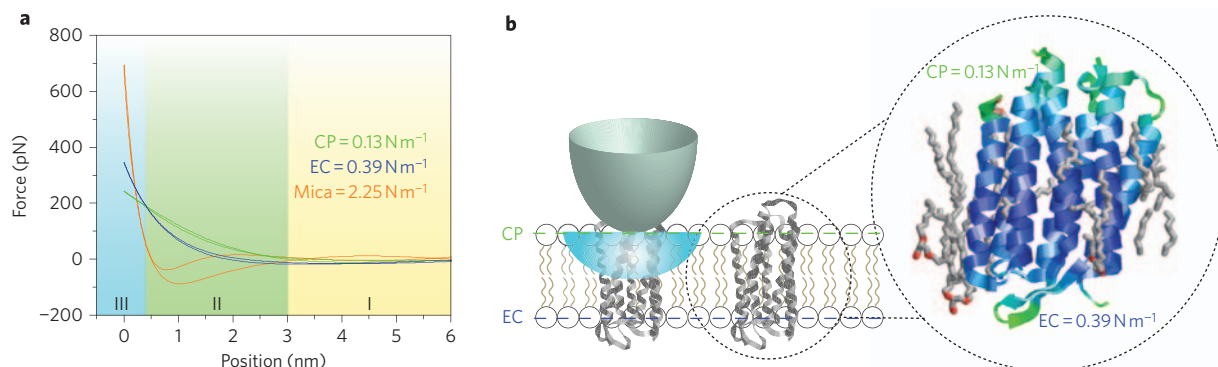


Figure 3 | Flexibility analysis of bacteriorhodopsin with high-speed force-distance curves. **a**, Force-distance curves recorded on the cytoplasmic side (green, CP), extracellular side (blue, EC) and mica (orange). The horizontal axis is split into three regions to illustrate where the tip and sample are separated (I), and where they are interacting through long-range (II) and short-range forces (III). The effective force constants are calculated from the slopes of the force-distance curves in region III. **b**, Schematic of the tip of an AFM interacting with a bR in the purple membrane. The transparent blue region illustrates the part of the membrane that predominantly contributes the tip-sample interaction. The enlarged cross-section of the structural model of bR is coloured according to B-factors¹⁸: the green and light blue colours of the transmembrane helices on the cytoplasmic side represent larger fluctuations and disorder compared to the extracellular side.

Table 1 | Effective force constants.

Sample/pH	6	7.8	9
Mica	2.09 ± 0.20	2.25 ± 0.40	1.86 ± 0.25
EC	0.32 ± 0.05	0.39 ± 0.05	0.43 ± 0.07
CP	0.08 ± 0.04	0.13 ± 0.04	0.17 ± 0.05

Measured on mica and the extracellular (EC) and cytoplasmic (CP) sides of the purple membrane at different pH values. The units of the force constants are N m^{-1} . The uncertainties are estimated from the ranges of more than 50 force constants measured on each sample. The salt concentration of the buffer is 300 mM (KCl).

between the cytoplasmic and extracellular surfaces qualitatively correlates to the B-factor map of bR in Fig. 3b, which shows increased disorder of the transmembrane helices near the cytoplasmic side¹⁸. Surprisingly, there is also a good degree of quantitative agreement with the effective force constants derived from neutron scattering experiments⁵, which characterize thermal fluctuations in the pico- to nanosecond timescale. Our AFM-based method, on the other hand, characterizes collective responses of the protein residues at the microsecond timescale, which is highly relevant to the dynamics

of proteins as it corresponds to the timescales of the large conformational changes required by their function.

The approximately threefold difference in the effective force constants of the cytoplasmic and extracellular sides of the native bR measured at physiologically relevant conditions provides further evidence of the role of increased structural flexibility in allowing conformational changes in the cytoplasmic side during the bR photocycle. These results may also provide insights into G-protein-coupled receptors possessing similar structural motifs with bR. In general, high-resolution and quantitative assessment of the structural flexibility of proteins near physiological conditions can help determine more accurate structure–function relationships, guide biomimetic design of synthetic molecular machines and identify targets to regulate protein function.

Methods

Cantilever design and characterization. L-THCs were fabricated from single-crystal silicon by using conventional manufacturing processes of commercial probes (MikroMasch), but with a custom geometry. The cantilever used in this work was 300 μm long, 20 μm wide and $\sim 2.0 \mu\text{m}$ thick. The tip offset distance was 25 μm . The free end of the cantilever was 60 μm wide. The radius of the tip was characterized by

transmission electron microscopy (TEM) and measured to be ~ 5 nm. The vertical spring constant of the cantilever used for the imaging experiments was 0.18 N m^{-1} (calibrated against thermomechanical noise). The force sensitivity of the torsional signal was calibrated according to the method of Sahin²¹ and was found to be 40 nN mV^{-1} . The flexural and torsional resonance frequencies in the imaging buffer were 7.7 and 176.1 KHz, respectively. The quality factors of these modes in buffer were measured from the width of the thermal noise peaks and were found to be 3.2 and 6.6 for the flexural and torsional modes, respectively. Owing to the low quality factors, the trajectory of the tip can deviate considerably from a sinusoid. We observed that small free vibration amplitudes (5–10 nm) needed to be used and that set point amplitudes should be chosen close to the free amplitude to keep the forces low and tip trajectory close to a sinusoid. Under these conditions, the stiffness of samples such as mica is significantly underestimated because the forces are not sufficient to indent the surface. In general, cantilevers with higher spring constants and higher quality factors are better suited for stiff materials¹³.

Sample preparation and buffer conditions. Purple membranes of *H. salinarum* (Sigma-Aldrich) were suspended in a stock solution of ultrapure water and diluted to $50 \mu\text{g ml}^{-1}$ in an adsorption buffer (300 mM KCl, 10 mM Tris/HCL, at pH 7.8). This solution (10 μl) was placed onto freshly cleaved mica for 30 min to allow membrane adsorption to the surface. Measurements were carried out under the same buffer conditions. Detailed protocols for AFM imaging and spectroscopy of native purple membranes can be found in ref. 27.

Atomic force microscopy. The AFM experiments were performed in the buffer conditions described above with a commercial instrument (Multimode SPM and Nanoscope V controller, Veeco Instruments). The L-THC was driven at its flexural resonance frequency with a set point amplitude of 5 nm, with the drive amplitude chosen such that peak interaction forces on the membranes were nominally 250 pN. This corresponds to ~ 5.5 nm free amplitude. The time-varying tip-sample force waveforms and corresponding elastic modulus values were calculated according to the procedures described in ref. 13. The measurement bandwidth was set to 1 kHz by averaging the waveforms over seven consecutive cycles. A description of contact mechanics models providing the elastic modulus values is given below. Flexibility maps are shown either as unprocessed images (Fig. 2c) or processed by a correlation averaging method²⁸ using SPIPTM software (Fig. 2d,e). In correlation averaging, a template area was defined and averaging performed over N (here $N = 100$) equivalently sized regions in the image that provided a best match (correlation) to this template.

Modelling of the tip-sample contact. Tip-sample interactions were predominantly determined by the long-range electrostatic and van der Waals forces, and short-range mechanical restoration forces. To estimate a local reduced elastic modulus we assumed that the long-range force components remained constant during the contact and used the following formula derived for a spherical tip indenting a semi-infinite planar sample with isotropic mechanical properties²⁹:

$$F_{\text{interaction}} = (4/3)E^* \sqrt{R}(d - d_0)^{3/2} + F_{\text{adh}} \quad (1)$$

where $F_{\text{interaction}}$ is the tip-sample force, E^* the reduced elastic modulus of the tip and the sample, R the tip radius, d_0 the surface rest position, $d - d_0$ the depth of indentation and F_{adh} the constant adhesion force during the contact. Note that the finite thickness of the purple membrane and its non-planar surface topography result in deviations from this formula. The effect of finite film thickness on our measurements can be best understood by comparing it to the contact radius $a = \sqrt{R(d - d_0)^{1/2}}$. In the presence of a Hertzian contact pressure distribution, the value of the stress in the sample beneath the surface reduces by 50% at a depth equal to the contact radius³⁰. The E^* values of 7 and 35 MPa for the cytoplasmic and extracellular sides of the purple membrane found in this work corresponds to contact diameters of 3.7 and 2.2 nm at a net repulsive force of 100 pN. Therefore, the tip is mainly interacting with the upper half of the membrane in either orientation. Furthermore, the flexibility maps presented in Fig. 2d,e exhibit spatial resolutions sufficient to resolve the triangular morphology of the bR trimers. This indicates that the contact radii on either side of the membrane may be smaller than those predicted by equation (1), which is likely due to the angstrom-scale corrugations on the proteins. In that case, the effect of membrane thickness on the measurements could be even smaller.

Received 12 November 2008; accepted 27 May 2009;
published online 28 June 2009

References

- Falke, J. J. & Koshland, D. E. Global flexibility in a sensory receptor—a site-directed cross-linking approach. *Science* **237**, 1596–1600 (1987).
- Frauenfelder, H., Sligar, S. G. & Wolynes, P. G. The energy landscapes and motions of proteins. *Science* **254**, 1598–1603 (1991).
- Frauenfelder, H., Petsko, G. A. & Tsernoglou, D. Temperature-dependent X-ray-diffraction as a probe of protein structural dynamics. *Nature* **280**, 558–563 (1979).

- Mittermaier, A. & Kay, L. E. New tools provide new insights in NMR studies of protein dynamics. *Science* **312**, 224–228 (2006).
- Zaccai, G. How soft is a protein? A protein dynamics force constant measured by neutron scattering. *Science* **288**, 1604–1607 (2000).
- Subramaniam, S., Gerstein, M., Oesterheld, D. & Henderson, R. Electron-diffraction analysis of structural changes in the photocycle of bacteriorhodopsin. *EMBO J.* **12**, 1–8 (1993).
- Rouso, I. *et al.* Microsecond atomic force sensing of protein conformational dynamics: implications for the primary light-induced events in bacteriorhodopsin. *Proc. Natl Acad. Sci. USA* **94**, 7937–7941 (1997).
- Dodson, G. & Verma, C. S. Protein flexibility: its role in structure and mechanism revealed by molecular simulations. *Cell. Mol. Life Sci.* **63**, 207–219 (2006).
- Clausen-Schaumann, H., Seitz, M., Krautbauer, R. & Gaub, H. E. Force spectroscopy with single bio-molecules. *Curr. Opin. Chem. Biol.* **4**, 524–530 (2000).
- Sulchek, T. A. *et al.* Dynamic force spectroscopy of parallel individual Mucin1-antibody bonds. *Proc. Natl Acad. Sci. USA* **102**, 16638–16643 (2005).
- Dietz, H., Berkemeier, F., Bertz, M. & Rief, M. Anisotropic deformation response of single protein molecules. *Proc. Natl Acad. Sci. USA* **103**, 12724–12728 (2006).
- Knowles, T. P. *et al.* Role of intermolecular forces in defining material properties of protein nanofibrils. *Science* **318**, 1900–1903 (2007).
- Sahin, O., Maganov, S., Su, C., Quate, C. F. & Solgaard, O. An atomic force microscope tip designed to measure time-varying nanomechanical forces. *Nature Nanotech.* **2**, 507–514 (2007).
- Martinez, N. F. *et al.* Bimodal atomic force microscopy imaging of isolated antibodies in air and liquids. *Nanotechnology* **19**, 384011 (2008).
- Preiner, J., Tang, J. L., Pastushenko, V. & Hinterdorfer, P. Higher harmonic atomic force microscopy: Imaging of biological membranes in liquid. *Phys. Rev. Lett.* **99**, 046102 (2007).
- Legleiter, J., Park, M., Cusick, B. & Kowalewski, T. Scanning probe acceleration microscopy (SPAM) in fluids: Mapping mechanical properties of surfaces at the nanoscale. *Proc. Natl Acad. Sci. USA* **103**, 4813–4818 (2006).
- Haupts, U., Tittor, J. & Oesterheld, D. Closing in on bacteriorhodopsin: progress in understanding the molecule. *Annu. Rev. Biophys. Biomol. Struct.* **28**, 367–399 (1999).
- Luecke, H., Schobert, B., Richter, H. T., Cartailler, J. P. & Lanyi, J. K. Structure of bacteriorhodopsin at 1.55 angstrom resolution. *J. Mol. Biol.* **291**, 899–911 (1999).
- Muller, D. J. & Engel, A. The height of biomolecules measured with the atomic force microscope depends on electrostatic interactions. *Biophys. J.* **73**, 1633–1644 (1997).
- Zhong, S. *et al.* Different interactions between the two sides of purple membrane with atomic force microscope tip. *Langmuir* **23**, 4486–4493 (2007).
- Sahin, O. Harnessing bifurcations in tapping-mode atomic force microscopy to calibrate time-varying tip-sample force measurements. *Rev. Sci. Instrum.* **78**, 103707 (2007).
- Parlak, Z. & Degertekin, F. L. Contact stiffness of finite size subsurface defects for atomic force microscopy: three-dimensional finite element modeling and experimental verification. *J. Appl. Phys.* **103**, 114910 (2008).
- Stark, M., Moller, C., Muller, D. J. & Guckenberger, R. From images to interactions: high-resolution phase imaging in tapping-mode atomic force microscopy. *Biophys. J.* **80**, 3009–3018 (2001).
- Alexiev, U., Marti, T., Heyn, M. P., Khorana, H. G. & Scherrer, P. Surface-charge of bacteriorhodopsin detected with covalently bound pH indicators at selected extracellular and cytoplasmic sites. *Biochemistry* **33**, 298–306 (1994).
- Engel, A. & Muller, D. J. Observing single biomolecules at work with the atomic force microscope. *Nature Struct. Biol.* **7**, 715–718 (2000).
- Muller, D. J., Fotiadis, D. & Engel, A. Mapping flexible protein domains at subnanometer resolution with the atomic force microscope. *FEBS Lett.* **430**, 105–111 (1998).
- Muller, D. J. & Engel, A. Atomic force microscopy and spectroscopy of native membrane proteins. *Nature Protoc.* **2**, 2191–2197 (2007).
- Patrick, D. L., Cee, V. J. & Beebe, T. P. Molecule corrals for studies of monolayer organic films. *Science* **265**, 231–234 (1994).
- Israelachvili, J. *Intermolecular and Surface Forces* (Academic Press, 2003).
- Johnson, K. L. *Contact Mechanics* (Cambridge Univ. Press, 2003).

Acknowledgements

This work was supported by the Rowland Junior Fellows program.

Additional information

Supplementary information accompanies this paper at www.nature.com/naturenanotechnology. Reprints and permission information is available online at <http://ngp.nature.com/reprintsandpermissions/>. Correspondence and requests for materials should be addressed to O.S.